HHS Public Access

Author manuscript

J Phys Chem Lett. Author manuscript; available in PMC 2022 March 18.

Published in final edited form as:

J Phys Chem Lett. 2021 October 07; 12(39): 9662–9671. doi:10.1021/acs.jpclett.1c02306.

Label-free Infrared Spectroscopic Imaging Reveals Heterogeneity of Beta Sheet Aggregates in Alzheimer's Disease

Matthew P. Confer, **Brooke M. Holcombe**, **Abigail G. Foes**, **John M. Holmquist**, **Savannah C. Walker**, **Sanghamitra Deb**, **Ayanjeet Ghosh***

Department of Chemistry and Biochemistry, University of Alabama, Tuscaloosa, AL-35401, USA.

Abstract

Aggregation of the beta amyloid (Aβ) protein into plaques is a pathological feature of Alzheimer's disease (AD). While amyloid aggregates have been extensively studied in vitro, their structural aspects and associated chemistry in the brain are not fully understood. In this report, we demonstrate using infrared spectroscopic imaging that Aβ plaques exhibit significant heterogeneities in terms of their secondary structure and phospholipid content. We show that the capabilities of discrete frequency infrared imaging (DFIR) are ideally suited for characterizing amyloid deposits in brain tissues and employ DFIR to identify non-plaque beta sheet aggregates distributed throughout brain tissues. We further demonstrate that phospholipid rich beta sheet deposits exist outside of plaques in all diseased tissues, indicating their potential clinical significance. This is the very first application of DFIR towards characterizing protein aggregates in AD brain and provides a rapid, label-free approach that allows us to uncover beta-sheet heterogeneities in the AD, which may be significant for targeted therapeutic strategies in future.

Graphical Abstract

***Corresponding Author:** ayanjeet.ghosh@ua.edu.

Supporting Information. The following files are available free of charge. IR images of plaques from postcentral gyrus and occipital lobe tissue sections, IR absorbance and beta sheet and phosphate ratio images of full tissue sections (normal and diseased precentral gyrus, postcentral gyrus and occipital lobe), IR spectra across plaque core, histogram of ratio image values and its second derivative, 100% spectral line for a single pixel under typical experimental conditions, second derivative of mean spectra of tissues, IHC images of phosphate rich regions in tissues, spectral fitting parameters. (PDF)

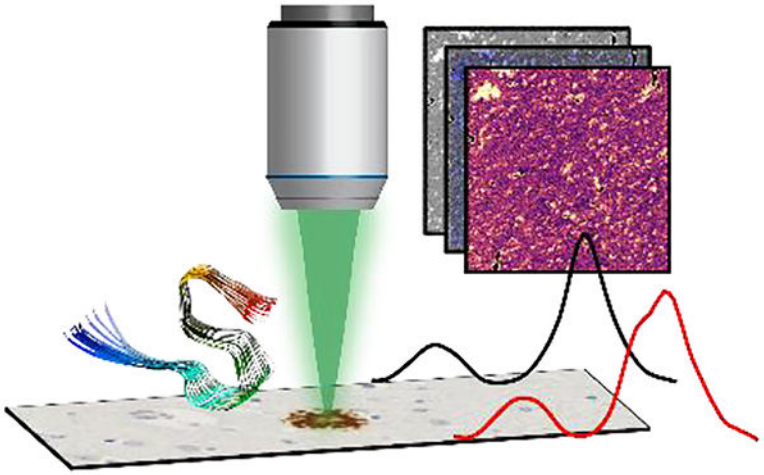

Keywords

Beta sheet; amyloid beta; infrared spectroscopy; chemical imaging; Alzheimer's disease

Aggregation of the amyloid beta (Aβ) protein into insoluble deposits or plaques is one of main pathological features of Alzheimer's disease (AD)[1–5]. However, the exact role of Aβ plaques in AD pathogenesis and onset of dementia is unclear[2, 4]. The aggregation of different Aβ isoforms in vitro has been studied at length both experimentally and computationally, and it is well known that that mature Aβ fibrils are extended parallel beta sheets[6–9], whereas Aβ oligomers may have a different secondary structure[10–14]. Furthermore, it is also known that all amyloid fibrils are also not equivalent: Aβ fibrils are polymorphic[7, 15–16], with variations in molecular structure associated with different morphologies of fibrils which not only exhibit different levels of neurotoxicity[8], but also have been shown to be associated with different stages of AD[17]. Hence there is growing evidence of chemical heterogeneities in Aβ deposits which may be linked to their role in AD. However, detailed structural information about Aβ assemblies in the human brain are lacking, and it is unclear to what extent different conformations identified in vitro persist in Aβ deposits in brain tissues and how their abundance correlates with AD. It is currently not known if morphologically similar plaques have the same chemical composition and environment for an individual patient or if there are variations between patients with different levels of neurological symptoms. Systematic studies of chemical composition of plaques, in human brain and their relationship with AD pathogenesis are yet to be undertaken.

One of the main reasons behind this gap in knowledge is the lack of suitable techniques capable of mapping the tissue chemistry. Fluorescence based approaches have been widely used to identify Aβ aggregates with different secondary structures (diffuse and beta sheet containing neuritic plaques)[18–19], but they require additional stains. Furthermore, immunohistochemical (IHC) staining using fluorophores often cannot be multiplexed to more than 2–3 labels due to spectral overlap. Solid state Nuclear Magnetic Resonance (ssNMR) is the technique of choice for structural characterization of amyloid fibrils[6, 20–22],

but cannot be extended to spatially resolved imaging in tissues. Chemical imaging approaches based on mass spectrometry have been applied to this task[23–24], but it is difficult to obtain quantitative assessment of secondary structures. Infrared (IR) spectroscopy is one of the most widely used spectroscopic techniques for investigating amyloid structure[25–27], and its capabilities can be harnessed to characterize the chemistry of plaques by augmenting it with optical imaging.

IR spectroscopic imaging is a promising technology that utilizes the inherent chemistry of the tissue for chemical contrast, wherein absorption of infrared light by vibrational modes of molecular constituents at characteristic wavelengths provides the contrast mechanism, thus offering a label-free chemical map of the tissue chemistry[28–34]. Each pixel contains an infrared absorption spectrum, which in turn provides a chemical fingerprint relatable to tissue constituents. In fact, Fourier Transform Infrared (FTIR) based imaging approaches have been applied to investigating Aβ plaques[35–39]. However, though IR imaging offers the desired contrast to explore the structural and chemical variations in amyloid aggregates ex-vivo, tabletop FTIR microscopes are not suitable for rapid scanning of large tissue specimens[40–41] which has limited applications on FTIR imaging to mostly proof-of-concept measurements and sample sizes of low statistical significance. In fact, the FTIR studies of Alzheimer's tissues have been essentially guided by histology and have focused only on plaques that can be identified through IHC and not the chemistry of the entire tissue. Raman microspectroscopy is another tool often employed for mapping tissue chemistry[42–44]; however, it suffers from similar limitations as FTIR imaging.

Recent technological developments in IR imaging, particularly using high power laser illumination sources have significantly expanded the capabilities of infrared spectroscopic imaging[40, 45]. In this report, we demonstrate, for the very first time, the capabilities of discrete frequency IR imaging (DFIR) using tunable quantum cascade laser (QCL) sources at discerning chemical variations in Aβ plaques in human Alzheimer's disease tissues. Our approach allows for tuning the laser to a few specific frequencies of interest; thus, the limitations of conventional FTIR imaging can be circumvented and chemical maps of entire tissue sections can be rapidly characterized. It should be noted that QCL sources are largely limited to the fingerprint spectral region (~1000–1800cm^{-1}), which in turn significantly reduces the spectral information accessible to DFIR. Hence meaningful applications of DFIR are essentially in systems where chemical information of interest can be obtained from the fingerprint region, such as tissues. In fact, the utility of the DFIR towards biomedical tissue imaging and characterizing polymers and functional materials like metal organic frameworks has been unequivocally demonstrated[40, 45–49]. In this report, we leverage the capabilities of DFIR to show that there are significant heterogeneities in the chemistry of Aβ aggregates, in plaques and non-plaque deposits. Our results indicate that besides plaques, the tissue contains additional beta sheet aggregates, which can have potential clinical implications. We also demonstrate the potential of DFIR imaging towards rapid, label-free mapping of all beta sheet aggregates and additional chemical variabilities in Alzheimer's tissues.

We first evaluated the capability of our instrumentation at identifying beta sheet aggregates by investigating a single formalin fixed paraffin embedded (FFPE) tissue specimen from

precentral gyrus of a 73-year old Alzheimer's patient (Biochain Institute, CA, USA). The presence and spatial locations of Aβ plaques in tissues was verified using IHC staining of adjacent sections with the MOAB-2 antibody[50]. MOAB is a pan-amyloid antibody that binds to multiple conformations of two major isoforms of Aβ, namely Aβ 1–40 and Aβ 1–42, including unaggregated protein, oligomeric assemblies and fibrillar aggregates[50–51]. This allows for identification of both dense-core plaques, which are typically beta-sheet rich, and also amorphous diffuse plaques, which are typically depleted in beta-sheet structures. Figure 1A shows the IHC stained image of a typical Aβ plaque.

The backbone amide I vibrations in proteins, which absorb between ~1600–1700 cm^{-1}, are sensitive to secondary structure, and localized spectra measured at different locations within a plaque (Figure 1B) exhibit clear differences in this region compared to spectra from non-plaque spatial locations (locations that do not exhibit IHC stained plaques). The beta sheet signature is evident in the spectra as a shoulder at ~1630cm^{-1}. The abundance of beta sheets in stained plaques can be better visualized by inspecting the intensity of this shoulder relative to the amide I peak, which occurs at ~1660cm^{-1}. We have used the ratio of the intensity at 1628 cm^{-1} to the amide I peak as the metric to map beta sheet aggregates. Similar ratios have been previously been used for mapping beta sheets in Alzheimer's brain tissue sections[35, 37–38]. We have also verified the fidelity of this metric, as described later. In this work, we have categorized the plaques, as identified through IHC staining, into three categories: cored, non-cored and diffuse. The cored Aβ plaques are expected to have fibrillar beta-sheet aggregates at the core[1, 38, 52], which is the dense central area of the plaque. Non-cored, compact plaques are also expected to contain beta sheets, as has been demonstrated before[38]. Diffuse plaques, on the other hand, contain amorphous deposits of the Aβ protein, and therefore are not expected to exhibit beta sheet signatures[1, 38, 52]. The IHC stained images and corresponding IR ratio images ($I_{1628}/(I_{1628} + I_{1660})$) of representative dense-core, non-cored, and diffuse plaques are shown in Figure 2A–L. Additional representative plaques from the tissue specimens from different brain locations (postcentral gyrus and occipital lobe) are shown in Figure S1 and S2, respectively. Spectral variation across the core of a plaque is shown in Figure S3. Full tissue IR absorbance images at 1628 and 1660 cm^{-1} are shown in Figures S4–S5.

The difference between the normalized average spectra of the plaques is shown in Figure 2M–O. The plaque shown in Figure 2A is a classic cored Aβ plaque, and we observe beta sheet signatures corresponding to the core (Figure 2B) as expected. However, the plaque shown in Figures 2C–D is also a cored plaque, but it does not contain significant beta sheet features at the core. Normalized average spectra of the plaques was calculated by averaging all pixels inside the plaque based on the stained image and normalizing these averaged spectra to the spectral intensity at 1660 cm^{-1}. The difference of the mean spectra of the plaques (Figure 2M) exhibits an intense peak located at 1636 cm^{-1}, typical of beta sheets. Absorption bands at ~1636cm^{-1} have been attributed in literature to intramolecular beta sheets, whereas amyloid fibrils are primarily constituted of intermolecular beta sheets, which are expected to absorb at lower wavenumbers. However, beta sheet absorption frequencies are variable, and can shift significantly depending on exact molecular structure[53–55]. Furthermore, the values in literature are typically from condensed phase measurements with

protein aggregates suspended in solution. Our measurements are in dehydrated, fixed tissues and do not contain any solvent, and that can further shift the vibrational frequencies, as it is well known that amide vibrational frequencies are sensitive to the solvent environment[56–58]. Therefore, our observations do not preclude the presence of intermolecular beta sheets.

The observation of no prominent beta sheet signature in the cored plaque in Figure 2C–D contrasts with the conventional idea that classic Aβ plaques contain a beta sheet core. We also observe beta sheet deposits outside the plaque boundary, indicated with black arrows, which we discuss in more detail later in the manuscript. The plaques shown in Figure 2E–H are examples of non-cored, compact plaques. Again, we observe that one of them contains beta sheets (Figure 2E and F), while the other does not (Figure 2G and H). This is also evidenced by the difference spectrum shown in Figure 2N. The same conclusion can be reached about diffuse plaques, shown in Figure 2I–L and Figure 2O. Non-plaque beta deposits (that is, outside the boundary of the plaque) are also observed near non-cored and diffuse plaques, which are indicated with black arrows and discussed later in the manuscript. These observations suggest that there can be variations in beta sheet content of Aβ plaques that is inconsistent with the expectation from their morphology. This has not been reported previously. Rak and coworkers have previously demonstrated that diffuse plaques do not exhibit any significant beta sheet signatures in mouse brain specimens[35]. More recent work by Röhr et. al.[38] has identified variations in secondary structure in different plaque types in human brain, but they did not observe a significant lack of beta sheet structure from neuritic plaque cores, or significant presence of beta sheets in diffuse plaques. Our results indicate that there can be more pronounced variations in plaque chemistry than previously reported. To ensure that this is not unique just to the plaques shown in Figure 2, a total of 227 plaques from three different brain locations (precentral gyrus, postcentral gyrus, occipital lobe) were investigated to verify the validity of the above observation. Quantitatively assigning plaques as either beta-sheet containing or beta-sheet depleted categories is somewhat challenging, because there exists no defined threshold intensity that demarcates normal and beta sheet rich spectra. One possible approach towards determining this baseline is to use spectra from non-plaque regions; however, as we discuss later, the tissues exhibit presence of small beta sheet deposits even in unstained spatial locations. Therefore, we determined the threshold by first calculating the histograms of the ratio images and consequently calculating their second derivatives[59–60]. The threshold point was selected to be the value corresponding to the second maxima of the second derivative of the histogram. The threshold ratio value thus determined was 0.25. The mean spectrum of all the pixels within the plaque boundary, as identified from IHC stained images, was then calculated, and the ratio value for the mean spectrum was determined. If the ratio value was above the threshold, the plaque was assigned to the beta-sheet containing group; otherwise, it was classified as beta-sheet depleted. Using this approach, we assigned plaques of each morphological subtypes (cored, non-cored and diffuse) to one of the above groups. The percent distributions of beta-sheet containing and depleted plaques for each morphological category is shown in Figure 2P. It can be seen that a significant fraction of cored and non-cored plaques lack beta sheets, whereas diffuse plaques often contain beta sheets, as determined from their average spectra. Representative IHC and IR images of other plaques exhibiting the above trend are shown in the Supplementary Information. A representative histogram, its second derivative, and

spectra that have ratio values above and below the threshold are shown in Figure S6. The spectral noise (reflected in the 100% line in the hyperspectral images) is also shown in Figure S6 to indicate that the variations between beta sheet containing and depleted spectra are significantly higher than the noise level. It is important to note in this context that morphological characterization of Aβ plaques is complex, and depending on complementary approaches, such as silver staining, other subtypes of plaques than categories mentioned above (cored, non-cored and diffuse) can be determined[52]. We also recognize that the choice of thresholding parameters can also influence the relative categorization of plaques. Based on the above results, it can nonetheless be concluded that morphologically similar plaques are not necessarily equivalent and can have secondary structure differences in terms of the average abundance of beta sheet deposits. This is a novel result and to the best of our knowledge, has never been identified previously. It has been conclusively demonstrated that Aβ can assume different secondary structures at different stages of aggregation and is not necessarily limited to fibrillar beta-sheets[14, 16–17, 21, 35, 38, 61]. Since the plaques do stain positive in IHC, but often lack beta sheet signatures in IR, we can conclude that cored and non-cored plaques can contain amorphous Aβ protein, which underscores the need to chemically characterize plaques in addition to morphological staining. Aβ plaques have been investigated with spectroscopic imaging techniques, such as FTIR and Raman microspectroscopies, but primarily in animal specimens; these approaches have been extended to human specimens only very recently, so the possibilities of peculiarities of AD pathology specific to human tissues cannot be ruled out. Lochocki et. al. have shown that there is no obvious Raman spectral signature that can be attributed to Aβ plaques[42], which indicates that for specific specimens, the secondary structure variations in plaques can be even more pronounced. We note that there can also be heterogeneities of interest within single plaques, which are not accounted for by our approach described above. This work focuses of identifying the differences between different plaques; intra-plaque variations in chemistry will be addressed in future work.

The difference spectra shown in Figure 2M–O point to additional chemical variations between plaques. The spectra contain additional peaks at ~1350 cm^{-1} and at ~1080 cm^{-1}. The first peak is challenging to assign; amide III vibrations, along with carboxylic acid vibrations typically absorb in this spectral range; additionally, the dependence of amide III modes on secondary structure is not well understood[54]. Hence, we focused on the second peak, which can be unequivocally attributed to phosphate groups, and its presence in the difference spectrum indicates variation in phosphate distribution between plaques. It is well known that Neurofibrillary tangles (NFTs), also a pathological feature of AD, involve aggregates of hyperphosphorylated tau[2, 52]. It has also been demonstrated that aggregated Aβ may trigger the hyperphosphorylation of tau, and it is believed that Aβ and phosphorylated tau coexist in neurons in AD brain. To investigate the distribution of phosphate species and their association with beta sheets, we compared spatial of maps of the phosphate band at 1080 cm^{-1} to beta sheet distributions. Phosphate intensities normalized to the amide I peak ($I_{1080}/(I_{1080} + I_{1660})$) for the cored plaques in Figure 2A–D are shown in Figure 3. The corresponding beta sheet ratio intensities, ($I_{1628}/(I_{1628} + I_{1660})$), from Figure 2 are also shown for comparison. For each image, the mean value is subtracted from all the pixels for clarity and enhanced contrast[62]. The full tissue images for both phosphate and

beta sheet ratios are presented in the Supporting Information (Figures S7 and S8). The IR absorbance images at 1080 cm^{-1} are shown in Figure S9. The IHC stained cored plaque in Figure 2A shows increased phosphate concentration in the plaque, as shown in Figure 3A, whereas the cored plaque Figure in 2C, which does not present a distinct beta sheet core, also contains significantly less phosphate in the plaque region (Figure 3B). It is known that Aβ associates with phospholipids, which could contribute to the enhanced phosphate signal in plaques[63–67]. Rak and coworkers have demonstrated presence of phospholipids along the periphery of neuritic plaques[35]. Surowka et.al. have also identified increased phosphate signals in Aβ plaque cores with FTIR microscopy, which they attributed to likely increased abundance of phospholipids[37]. Therefore, we can tentatively attribute these signals to phospholipids. However, it is important to note that all of the previous reports that have identified phospholipids in tissues have used frozen specimens. The formalin fixed paraffin embedded (FFPE) specimens studied in this work were washed with hexane for deparaffinizing, which is also expected to remove lipids. Hughes and coworkers have suggested that not all lipids are removed during deparaffinization[68]; more recently Lochocki et. al. have mapped lipid distributions in FFPE brain sections with Raman microscopy[42]. Therefore, this suggests the phospholipids observed herein are structurally integrated into the plaque beta sheets. Phospholipid mediated aggregation pathways[63–65] for Aβ are known, and observation of structurally integrated phospholipids in plaque cores would support this hypothesis. Essentially, if aggregation of Aβ is mediated by phospholipids, then we can expect to observe colocalization and strong correlation between phosphate and beta sheet intensities.

To understand the accumulation of phosphorylated species and its correlation to beta sheets in plaques, we investigated the 227 plaques from the three tissue specimens. The threshold value, as described earlier, was used to determine if the spectrum of a particular pixel within plaque boundaries contained beta sheets. The average of such beta sheet containing spectra was then calculated, and the phosphate and beta sheet ratios of the mean spectrum were evaluated. The correlation of the phosphate and beta sheet intensities, as described above, are shown in Figure 3E. Interestingly, we do not find significant positive correlation between beta sheets and phosphate band intensities in plaques. This implies that there can be phosphate rich pixels that do not contain beta sheets, and vice versa, suggesting that prevalence of phosphate moieties in plaques is not always related to beta sheet structures, and hence can have varied origins. Recent studies have identified the existence of phosphorylated Aβ in AD plaques[69–70] and phosphorylation is believed to be possible trigger for aggregation and consequent neurotoxicity of Aβ. Therefore, we acknowledge that the phosphate species associated with the plaque core can also arise in part from hyperphosphorylated Aβ, which can exist in non-beta sheet secondary structures. We also note that the plaques were not separated into morphological subtypes for this analysis and exploring phosphate abundances in specific subtypes of plaques may reveal more meaningful correlations. We aim to address this in future work. Nevertheless, taken together, these results are indicative of significant chemical heterogeneity in Aβ plaques not only in terms protein secondary structure but also with respect to phosphate and/or phospholipid content. Understanding the chemical variabilities between different aggregates will not only

advance our knowledge of the molecular chemistry of AD but also potentially unlock the development of targeted therapeutics for specific plaques.

These results underscore the need for expanding spectroscopic chemical imaging to investigating larger sample sizes, which will reveal a comprehensive picture of beta sheet chemistry of plaques and its heterogeneity. Furthermore, tissue locations outside of plaques can also offer relevant chemical insights. Specifically, we observe that non-plaque regions of the tissue specimens can also exhibit presence of small beta sheet aggregates, as seen in Figure 2 (indicated with arrows) and also in Figure 3. It is important to determine if these beta sheet aggregates are unique to plaque microenvironments or are more abundant throughout tissues to assess their role and relevance to AD. This necessitates hyperspectral scans of whole tissues, which entails significantly increased measurement times that can be challenging for common benchtop FTIR microscopes, as has been demonstrated by Yeh et. al[40]. Using tunable quantum cascade lasers as illumination sources in infrared microscopes allows for acquiring images at specific discrete frequencies of interest. As a result, the ratio depicted in Figures 2 and 3 can be generated by simply acquiring two images. However, the spectral space can be effectively reduced only when the same information can be obtained from specific frequencies. This can be difficult for understanding protein secondary structures, as amide I vibrations are convolutions of multiple bands from different protein secondary structures[26, 54], and simple intensity ratios may not always reflect the beta sheet populations accurately. In fact, spectral deconvolution through curve fitting or calculating second derivative spectra is often employed for studying secondary structures with infrared spectroscopy[54]. Hence, the primary task for transitioning to discrete frequency measurements is identifying discrete frequency-based metrics that can predict beta sheet populations with reasonable accuracy. Therefore, to evaluate if the beta sheet IR ratio, $(I_{1628}/(I_{1628} + I_{1660}))$, is truly representative of the actual beta sheet content, the spectral region from 1600–1700 cm^{-1} was fitted to 3 peaks for all pixels of the three tissue specimens, totaling over 15 million spectra. Although the amide I band is typically fitted to 4 or more peaks[37, 54], we observed that the mean second derivative spectrum of the tissue specimens exhibited 3 underlying peak signatures (Figure S10). Furthermore, a 3-peak fitting model adequately identifies the beta sheet population and fitting with additional peaks does not offer any significant improvement. The peak fitted beta sheet ratio and spectral intensity beta sheet ratio for representative regions of diseased precentral gyrus, postcentral gyrus, and occipital lobe are presented in Figure 4A–F. A representative fit spectrum is shown in Figure 4G and fitting parameters are shown in Table S1. The beta sheet containing pixels correspond extremely well between the fitted and spectral intensity data for all tissues, confirming that that the spectral intensity ratio is representative of beta sheet content. This is a significant result, as it indicates that the results from acquiring an entire spectrum and consequent deconvolution can be accurately approximated by measuring the IR intensity at two frequencies. This enables us to use discrete frequency measurements to map beta sheet aggregates over entire tissue specimens, which reduces the measurement time and data size by orders of magnitude, and reveals overlooked facets of tissue chemistry, as shown below.

The small non-plaque beta sheet deposits observed in Figures 2 and 3 were identified in all tissue samples in the ratio images and can be clearly seen in Figure 4. These deposits

were not found to be confined to plaque microenvironments specifically and are distributed throughout the tissues. The full tissue images are shown in the Supporting Information (Figure S7). To evaluate the relative abundance of these deposits in diseased and normal tissues, the average percentage of beta sheet rich pixels were calculated for three 1 mm^2 areas that exclude stained Aβ deposits for each specimen (Figure 4H). The diseased precentral gyrus and occipital lobe specimens contain a greater number of these small, non-plaque, beta sheets than the corresponding normal controls. The normal postcentral gyrus appears to have more abundance of these beta sheet deposits as the diseased tissue. This may be due to natural variations per person and per tissue sample.

Some of these small beta sheet deposits correspond well to nuclei in in the IHC images, and hence can be attributed to glial cells. The role of peripheral cells in AD pathology is debated and more work is necessary to understand the implications of beta sheet aggregates in glial cells[71]. Another possible explanation of these beta sheet deposits is tau aggregates. However, the majority of these deposits lack the characteristic morphology of tau aggregate rich neurofibrillary tangles (NFTs)[2, 52]; moreover, tau aggregates are intracellular, and not all these deposits correspond to cellular or neuronal locations. This points to the possibility that these aggregates could be Aβ that are not stained by IHC, or deposits of other proteins that misfold into plaques in AD. MOAB-2 is a pan-amyloid antibody that recognizes unaggregated, oligomeric, and fibrillar forms of synthetic Aβ42 and Aβ40[50–51]. Therefore, these deposits can arise from other isoforms of Aβ which would stain negative with MOAB-2. The presence of these non-plaque, unstained, beta sheet deposits in human AD brain tissue has not been reported in previous vibrational microscopy studies. A possible reason for this is that FTIR and Raman microspectroscopy based techniques have focused mostly on stained plaques and not always mapped entire tissue samples, which arises from the limitations of their experimental implementations. While the precise origins and clinical implications of the non-plaque beta sheet aggregates are unclear, the picture that emerges from these results point towards significant heterogeneity in the origin of beta sheets in AD brain, which underscores the necessity to understand protein secondary structures in ex-vivo brain specimens to further our understanding of AD pathology.

One key advantage of DFIR is spectral multiplexing: signatures for additional chemical markers can be readily incorporated by acquiring images at their specific wavenumbers. Hence the association of these non-plaque aggregates can be investigated by simply acquiring an image at the phosphate absorption wavenumber. Similar to plaques, the non-plaque beta sheet aggregates also do not show any significant colocalization with phosphates, with some notable exceptions. Phosphate rich regions were found in each diseased tissue all of which also exhibit beta sheet signal (Figure 5). Full tissue RGB overlay images are shown in the Supporting Information (Figures S7–S8). None of the deposits are Aβ positive in the IHC images (Figure S11), and their spatial distributions are not consistent with known plaque and NFT morphologies. These aggregates are present only in diseased tissue and do not appear in the normal control specimens, which points to their potential clinical significance. These deposits are not obviously assignable to any of the lesions typically associate with Alzheimer's disease, and to the best of our knowledge have not been reported before. There is increasing evidence that lipids play a key role in AD; upregulation of brain lipid metabolism is related to AD progression[66–67]. Changes

in phospholipid distributions in AD mouse models and the correlations with plaques have been identified with mass spectrometry[72–74]. However, none have identified integration of lipids and beta sheet aggregates. This is the first study to show the colocalization between beta sheets and phospholipids in non-plaque aggregates. Further work with larger sample sizes is necessary to precisely investigate the clinical implications of these aggregates and whether the aggregation follows a phospholipid mediated pathway, which we aim to address in future. Nonetheless these results point to understanding lipid-protein interactions as a potentially significant mechanism in AD pathogenesis.

We propose discrete frequency IR as a viable approach to interrogate protein structures and their phospholipid associations in AD brain tissues. To unequivocally demonstrate the applicability and advantages of this approach, we have imaged a ~16×24 mm^2 normal brain tissue section from the frontal lobe, shown in Figure 6. To map phosphate and beta sheet distributions, we acquired three images at 1080 cm^{-1}, 1628 cm^{-1} and 1660 cm^{-1}. The total image acquisition time is approximately 120 minutes at ~40 minutes per wavenumber. In contrast, a tissue of this spatial dimension would take more than a few days even with the most advanced implementations of FTIR microscopes and would result in file sizes of ~150GB and above. In contrast, the exact same information in furnished by our discrete frequency approach in merely a fraction of the time and data size.

In summary, we have demonstrated that there exist significant heterogeneities in beta sheet aggregates in AD brain tissues. Morphologically similar Aβ plaques can have significant variations in beta sheet content and in colocalized phosphate signals. Numerous small beta sheet deposits are also observed distributed throughout the tissues which do not stain positive in the IHC images and appear to be more abundant in diseased specimens. Some of these aggregates strongly colocalize with phosphate moieties and are only observed in diseased tissues. The precise origins and clinical implications of these aggregates, and the chemical heterogeneity thereof, is not clear and warrants further investigation. We demonstrate that discrete frequency infrared imaging is ideally suited for this challenge, providing rapid mapping of beta sheet aggregates over large tissue domains. Due to the timescale and data quantities required for conventional vibrational microscopies, studies are generally guided by histological staining and only stained areas are imaged and/or analyzed. Spectroscopic mapping guided solely by histological staining can overlook important facets of tissue chemistry, as evidenced by the results reported here. The key advantage of DFIR over conventional FTIR microspectroscopy is that only the wavenumbers of interest need to be acquired, reducing both the time and data size. While we have chosen to investigate phosphate associations with beta sheets in this report, DFIR can be easily extended to explore other chemical signatures of interest. Stimulated Raman scattering (SRS) based discrete frequency approaches have already seen application in characterizing Aβ aggregates in AD tissue[75], and we believe that the approaches described herein will be ideal complements to SRS. The ability to rapidly map out chemistry beyond histologically stained plaques to entire tissue sections has the potential to advance our fundamental knowledge of the molecular pathology of Alzheimer’s disease and can be key to development of future therapeutic strategies.

Experimental Methods

Formalin fixed paraffin embedded (FFPE) human precentral gyrus, postcentral gyrus, and occipital lobe diseased and normal tissues were purchased from Biochain Institute. The frontal lobe tissue specimen was purchased from Advanced Tissue Services, Tucson. The postmortem tissue specimens studied in this report were deidentified and were determined to be not human subjects research by the Office of Research Compliance at the University of Alabama. These tissues were deparaffinized in hexane for 24 hours before storage under mild vacuum. For IHC, sections adjacent to those used for infrared measurements were stained with the anti-amyloid MOAB-2 antibody (Sigma Aldrich) at the University of Alabama Birmingham pathology core research lab. IR images were acquired using a homebuilt confocal IR microscope. The microscope design is based upon work published by Bhargava and coworkers[40–41, 45]. The microscope uses a Quantum Cascade Laser (Block Engineering), tunable from 1000–1800 cm^{-1}, as the illumination source, a TE cooled mercury cadmium telluride (MCT) detector (Boston Electronics) and is equipped with a 0.74NA objective. Hyperspectral IR images were acquired for the spectral range 1000–1752 cm^{-1}, at 4 cm^{-1} spectral resolution and a pixel size of 2 microns. All measurements were made in transflection mode on infrared reflective low-emissivity slides (Kevley Technologies). The discrete frequency images were aligned using the image processing toolbox in MATLAB prior to generating hyperspectral image stacks and ratioing to mitigate any artifacts from stage drifts and inaccuracies during scanning. Optical images of stained tissues were acquired at 40x magnification using a Nanozoomer slide scanner at the Carl R. Woese Institute for Genomic Biology (IGB), University of Illinois, Urbana-Champaign. All the fitting procedures, image registration and analysis were carried out using the MATLAB software.

Supplementary Material

Refer to Web version on PubMed Central for supplementary material.

Acknowledgments.

This work was supported by the National Institutes of Health (Award 1 R35 GM138162 to A.G.). The authors thank Dr. Kevin Yeh and Dr. Rohit Bhargava for their help with the infrared microscope instrumentation, and Dr. Dezhi Wang at UAB Pathology Core Facility for help with IHC staining.

References

1. Serrano-Pozo A; Frosch MP; Masliah E; Hyman BT Neuropathological alterations in Alzheimer disease. Cold Spring Harb Perspect Med 2011, 1 (1), a006189–a006189. [PubMed: 22229116]
2. Perl DP Neuropathology of Alzheimer's disease. Mt Sinai J Med 2010, 77 (1), 32–42. [PubMed: 20101720]
3. Murphy MP; LeVine H 3rd. Alzheimer's disease and the amyloid-beta peptide. J Alzheimers Dis 2010, 19 (1), 311–323. [PubMed: 20061647]
4. Iadanza MG; Jackson MP; Hewitt EW; Ranson NA; Radford SE A new era for understanding amyloid structures and disease. Nature Reviews Molecular Cell Biology 2018, 19 (12), 755–773. [PubMed: 30237470]
5. Cline EN; Bicca MA; Viola KL; Klein WL The Amyloid-β Oligomer Hypothesis: Beginning of the Third Decade. J Alzheimers Dis 2018, 64 (s1), S567–S610. [PubMed: 29843241]

6. Tycko R Solid-state NMR studies of amyloid fibril structure. Annu Rev Phys Chem 2011, 62, 279–299. [PubMed: 21219138]
7. Tycko R Amyloid polymorphism: structural basis and neurobiological relevance. Neuron 2015, 86 (3), 632–645. [PubMed: 25950632]
8. Petkova AT; Leapman RD; Guo Z; Yau WM; Mattson MP; Tycko R Self-propagating, molecular-level polymorphism in Alzheimer's beta-amyloid fibrils. Science 2005, 307, 262. [PubMed: 15653506]
9. Paul TJ; Hoffmann Z; Wang C; Shanmugasundaram M; DeJoannis J; Shekhtman A; Lednev IK; Yadavalli VK; Prabhakar R Structural and Mechanical Properties of Amyloid Beta Fibrils: A Combined Experimental and Theoretical Approach. The Journal of Physical Chemistry Letters 2016, 7 (14), 2758–2764. [PubMed: 27387853]
10. Ahmed M; Davis J; Aucoin D; Sato T; Ahuja S; Aimoto S; Elliott JI; Van Nostrand WE; Smith SO Structural conversion of neurotoxic amyloid-beta(1–42) oligomers to fibrils. Nat Struct Mol Biol 2010, 17 (5), 561–567. [PubMed: 20383142]
11. Cerf E; Sarroukh R; Tamamizu-Kato S; Breydo L; Derclaye S; Dufrêne Yves F.; Narayanaswami V; Goormaghtigh E; Ruysschaert J-M; Raussens V Antiparallel β-sheet: a signature structure of the oligomeric amyloid β-peptide. Biochemical Journal 2009, 421 (3), 415–423.
12. Lee SJC; Nam E; Lee HJ; Savelieff MG; Lim MH Towards an understanding of amyloid-β oligomers: characterization, toxicity mechanisms, and inhibitors. Chemical Society Reviews 2017, 46 (2), 310–323. [PubMed: 27878186]
13. Xu J; Zhang JZH; Xiang Y Molecular Dynamics Simulation and Computational Two-Dimensional Infrared Spectroscopic Study of Model Amyloid β-Peptide Oligomers. The Journal of Physical Chemistry A 2013, 117 (29), 6373–6379. [PubMed: 23641734]
14. Mehrazma B; Rauk A Exploring Amyloid-β Dimer Structure Using Molecular Dynamics Simulations. The Journal of Physical Chemistry A 2019, 123 (22), 4658–4670. [PubMed: 31082235]
15. Close W; Neumann M; Schmidt A; Hora M; Annamalai K; Schmidt M; Reif B; Schmidt V; Grigorieff N; Fändrich M Physical basis of amyloid fibril polymorphism. Nature Communications 2018, 9 (1), 699.
16. Härd T Amyloid Fibrils: Formation, Polymorphism, and Inhibition. The Journal of Physical Chemistry Letters 2014, 5 (3), 607–614. [PubMed: 26276617]
17. Qiang W; Yau W-M; Lu J-X; Collinge J; Tycko R Structural variation in amyloid-β fibrils from Alzheimer's disease clinical subtypes. Nature 2017, 541, 217. [PubMed: 28052060]
18. Hualong F; Mengchao C Fluorescent Imaging of Amyloid-β Deposits in Brain: An Overview of Probe Development and a Highlight of the Applications for In Vivo Imaging. Current Medicinal Chemistry 2018, 25 (23), 2736–2759. [PubMed: 29446721]
19. Dalal V; Bhattacharya M; Narang D; Sharma PK; Mukhopadhyay S Nanoscale Fluorescence Imaging of Single Amyloid Fibrils. The Journal of Physical Chemistry Letters 2012, 3 (13), 1783–1787. [PubMed: 26291859]
20. Eisenberg DS; Sawaya MR Structural Studies of Amyloid Proteins at the Molecular Level. Annual Review of Biochemistry 2017, 86 (1), 69–95.
21. Martial B; Lefèvre T; Auger M Understanding amyloid fibril formation using protein fragments: structural investigations via vibrational spectroscopy and solid-state NMR. Biophys Rev 2018, 10 (4), 1133–1149. [PubMed: 29855812]
22. Patel HR; Pithadia AS; Brender JR; Fierke CA; Ramamoorthy A In Search of Aggregation Pathways of IAPP and Other Amyloidogenic Proteins: Finding Answers through NMR Spectroscopy. The Journal of Physical Chemistry Letters 2014, 5 (11), 1864–1870. [PubMed: 26273866]
23. Erik P; Niklas M; Ulf A; Kaj B; Henrik Z Novel Aβ Isoforms in Alzheimer's Disease - Their Role in Diagnosis and Treatment. Current Pharmaceutical Design 2011, 17 (25), 2594–2602. [PubMed: 21728980]
24. Kaya I; Brinet D; Michno W; Başkurt M; Zetterberg H; Blenow K; Hanrieder J Novel Trimodal MALDI Imaging Mass Spectrometry (IMS3) at 10 μm Reveals Spatial Lipid and

Peptide Correlates Implicated in Aβ Plaque Pathology in Alzheimer's Disease. ACS Chemical Neuroscience 2017, 8 (12), 2778–2790. [PubMed: 28925253]

25. Sarroukh R; Goormaghtigh E; Ruysschaert J-M; Raussens V ATR-FTIR: A "rejuvenated" tool to investigate amyloid proteins. Biochimica et Biophysica Acta (BBA) - Biomembranes 2013, 1828 (10), 2328–2338. [PubMed: 23746423]
26. Moran SD; Zanni MT How to Get Insight into Amyloid Structure and Formation from Infrared Spectroscopy. The Journal of Physical Chemistry Letters 2014, 5 (11), 1984–1993. [PubMed: 24932380]
27. Tycko R Molecular Structure of Aggregated Amyloid-β: Insights from Solid-State Nuclear Magnetic Resonance. Cold Spring Harb Perspect Med 2016, 6 (8).
28. Reddy RK; Walsh MJ; Schulmerich MV; Carney PS; Bhargava R High-Definition Infrared Spectroscopic Imaging. Appl. Spectrosc 2013, 67 (1), 93. [PubMed: 23317676]
29. Nasse MJ; Walsh MJ; Mattson EC; Reininger R; Kajdacsy-Balla A; Macias V; Bhargava R; Hirschmugl CJ High-Resolution Fourier-Transform Infrared Chemical Imaging with Multiple Synchrotron Beams. Nat. Methods 2011, 8 (5), 413. [PubMed: 21423192]
30. Bhargava R Infrared Spectroscopic Imaging: The next Generation. Appl. Spectrosc 2012, 66, 1091. [PubMed: 23031693]
31. Baker MJ; Trevisan J; Bassan P; Bhargava R; Butler HJ; Dorling KM; Fielden PR; Fogarty SW; Fullwood NJ; Heys KA; Hughes C; Lasch P; Martin-Hirsch PL; Obinaju B; Sockalingum GD; Sulé-Suso J; Strong RJ; Walsh MJ; Wood BR; Gardner P; Martin FL Using Fourier transform IR spectroscopy to analyze biological materials. Nat. Protocols 2014, 9 (8), 1771–1791. [PubMed: 24992094]
32. Choi S; Birarda G Protein Mixture Segregation at Coffee-Ring: Real-Time Imaging of Protein Ring Precipitation by FTIR Spectromicroscopy. The Journal of Physical Chemistry B 2017, 121 (30), 7359–7365. [PubMed: 28692273]
33. Sakabe T; Yamazaki S; Hasegawa T Analysis of Cross-Section Structure of a Polymer Wrapping Film Using Infrared Attenuated Total Reflection Imaging Technique with an Aid of Chemometrics. The Journal of Physical Chemistry B 2010, 114 (20), 6878–6885. [PubMed: 20443583]
34. Hu J; Tashiro K Time-Resolved Imaging of the Phase Transition in the Melt-Grown Spherulites of Isotactic Polybutene-1 as Detected by the Two-Dimensional Polarized IR Imaging Technique. The Journal of Physical Chemistry B 2016, 120 (20), 4689–4698. [PubMed: 27149425]
35. Rak M; Del Bigio MR; Mai S; Westaway D; Gough K Dense-core and diffuse Aβ plaques in TgCRND8 mice studied with synchrotron FTIR microspectroscopy. Biopolymers 2007, 87 (4), 207–217. [PubMed: 17680701]
36. Liao CR; Rak M; Lund J; Unger M; Platt E; Albensi BC; Hirschmugl CJ; Gough KM Synchrotron FTIR reveals lipid around and within amyloid plaques in transgenic mice and Alzheimer's disease brain. Analyst 2013, 138 (14), 3991–3997. [PubMed: 23586070]
37. Surowka AD; Pilling M; Henderson A; Boutin H; Christie L; Szczerbowska-Boruchowska M; Gardner P FTIR imaging of the molecular burden around Aβ deposits in an early-stage 3-Tg-APP-PSP1-TAU mouse model of Alzheimer's disease. Analyst 2017, 142 (1), 156–168.
38. Röhr D; Boon BDC; Schuler M; Kremer K; Hoozemans JJM; Bouwman FH; El-Mashtoly SF; Nabers A; Großerueschkamp F; Rozemuller AJM; Gerwert K Label-free vibrational imaging of different Aβ plaque types in Alzheimer's disease reveals sequential events in plaque development. Acta Neuropathologica Communications 2020, 8 (1), 222. [PubMed: 33308303]
39. Benseny-Cases N; Klementieva O; Cotte M; Ferrer I; Cladera J Microspectroscopy (μFTIR) Reveals Co-localization of Lipid Oxidation and Amyloid Plaques in Human Alzheimer Disease Brains. Analytical Chemistry 2014, 86 (24), 12047–12054. [PubMed: 25415602]
40. Yeh K; Lee D; Bhargava R Multicolor Discrete Frequency Infrared Spectroscopic Imaging. Analytical Chemistry 2019, 91 (3), 2177–2185. [PubMed: 30605317]
41. Yeh K; Kenkel S; Liu J-N; Bhargava R Fast Infrared Chemical Imaging with a Quantum Cascade Laser. Analytical Chemistry 2015, 87 (1), 485–493. [PubMed: 25474546]

42. Lochocki B; Morrema THJ; Ariese F; Hoozemans JJM; de Boer JF The search for a unique Raman signature of amyloid-beta plaques in human brain tissue from Alzheimer's disease patients. Analyst 2020, 145 (5), 1724–1736. [PubMed: 31907497]
43. Surmacki J; Musial J; Kordek R; Abramczyk H Raman imaging at biological interfaces: applications in breast cancer diagnosis. Molecular Cancer 2013, 12 (1), 48. [PubMed: 23705882]
44. Lu F-K; Calligaris D; Olubiyi OI; Norton I; Yang W; Santagata S; Xie XS; Golby AJ; Agar NYR Label-Free Neurosurgical Pathology with Stimulated Raman Imaging. Cancer Research 2016, 76 (12), 3451–3462. [PubMed: 27197198]
45. Mittal S; Yeh K; Leslie LS; Kenkel S; Kajdacsy-Balla A; Bhargava R Simultaneous cancer and tumor microenvironment subtyping using confocal infrared microscopy for all-digital molecular histopathology. Proceedings of the National Academy of Sciences 2018, 115 (25), E5651.
46. Hughes C; Clemens G; Bird B; Dawson T; Ashton KM; Jenkinson MD; Brodbelt A; Weida M; Fotheringham E; Barre M; Rowlette J; Baker MJ Introducing Discrete Frequency Infrared Technology for High-Throughput Biofluid Screening. Scientific Reports 2016, 6 (1), 20173. [PubMed: 26842132]
47. Phal Y; Yeh K; Bhargava R Concurrent Vibrational Circular Dichroism Measurements with Infrared Spectroscopic Imaging. Analytical Chemistry 2021, 93 (3), 1294–1303. [PubMed: 33320538]
48. Ghosh A; Mukherjee P; Deb S; Bhargava R Mapping Solvation Environments in Porous Metal–Organic Frameworks with Infrared Chemical Imaging. The Journal of Physical Chemistry Letters 2017, 8 (21), 5325–5330. [PubMed: 29023128]
49. Mukherjee P; Ghosh A; Spegazzini N; Lamborn MJ; Monwar MM; DesLauriers PJ; Bhargava R Relating Post-yield Mechanical Behavior in Polyethylenes to Spatially Varying Molecular Deformation Using Infrared Spectroscopic Imaging: Homopolymers. Macromolecules 2018, 51 (10), 3836–3844.
50. Youmans KL; Tai LM; Kanekiyo T; Stine WB Jr; Michon S-C; Nwabuisi-Heath E; Manelli AM; Fu Y; Riordan S; Eimer WA; Binder L; Bu G; Yu C; Hartley DM; LaDu MJ Intraneuronal Aβ detection in 5xFAD mice by a new Aβ-specific antibody. Molecular Neurodegeneration 2012, 7 (1), 8. [PubMed: 22423893]
51. Chidlow G; Wood JPM; Manavis J; Finnie J; Casson RJ Investigations into Retinal Pathology in the Early Stages of a Mouse Model of Alzheimer's Disease. Journal of Alzheimer's Disease 2017, 56, 655–675.
52. Wippold FJ; Cairns N; Vo K; Holtzman DM; Morris JC Neuropathology for the Neuroradiologist: Plaques and Tangles. American Journal of Neuroradiology 2008, 29 (1), 18. [PubMed: 17925367]
53. Lomont JP; Ostrander JS; Ho J-J; Petti MK; Zanni MT Not All β-Sheets Are the Same: Amyloid Infrared Spectra, Transition Dipole Strengths, and Couplings Investigated by 2D IR Spectroscopy. The Journal of Physical Chemistry B 2017, 121 (38), 8935–8945. [PubMed: 28851219]
54. Barth A Infrared spectroscopy of proteins. Biochimica et Biophysica Acta (BBA) - Bioenergetics 2007, 1767 (9), 1073–1101. [PubMed: 17692815]
55. Barth A; Zscherp C What vibrations tell us about proteins. Q Rev Biophys 2002, 35 (4), 369–430. [PubMed: 12621861]
56. DeCamp MF; DeFlores L; McCracken JM; Tokmakoff A; Kwac K; Cho M Amide I Vibrational Dynamics of N-Methylacetamide in Polar Solvents: The Role of Electrostatic Interactions. The Journal of Physical Chemistry B 2005, 109 (21), 11016–11026. [PubMed: 16852342]
57. Haldar T; Kashid SM; Deb P; Kesh S; Bagchi S Pick and Choose the Spectroscopic Method to Calibrate the Local Electric Field inside Proteins. The Journal of Physical Chemistry Letters 2016, 7 (13), 2456–2460. [PubMed: 27295386]
58. Reppert M; Tokmakoff A Electrostatic frequency shifts in amide I vibrational spectra: Direct parameterization against experiment. The Journal of Chemical Physics 2013, 138 (13), 134116. [PubMed: 23574217]
59. Guzmán C; Bagga M; Kaur A; Westermarck J; Abankwa D ColonyArea: An ImageJ Plugin to Automatically Quantify Colony Formation in Clonogenic Assays. PLOS ONE 2014, 9 (3), e92444. [PubMed: 24647355]

60. Friedman JM Fourier-filtered van der Waals contact surfaces: accurate ligand shapes from protein structures. Protein Engineering, Design and Selection 1997, 10 (8), 851–863.
61. Ahmed M; Davis J; Aucoin D; Sato T; Ahuja S; Aimoto S; Elliott JI; Van Nostrand WE; Smith SO Structural conversion of neurotoxic amyloid-β1–42 oligomers to fibrils. Nat Struct Mol Biol 2010, 17 (5), 561–567. [PubMed: 20383142]
62. Jarrett K, Kavukcuoglu K, Ranzato M, LeCun Y What is the best multi-stage architecture for object recognition? 2009 IEEE 12th International Conference on Computer Vision (ICCV), Kyoto 2009 2146–2153.
63. Kosicek M; Hecimovic S Phospholipids and Alzheimer's disease: alterations, mechanisms and potential biomarkers. Int J Mol Sci 2013, 14 (1), 1310–1322. [PubMed: 23306153]
64. Fabiani C; Antollini SS Alzheimer's Disease as a Membrane Disorder: Spatial Cross-Talk Among Beta-Amyloid Peptides, Nicotinic Acetylcholine Receptors and Lipid Rafts. Frontiers in Cellular Neuroscience 2019, 13 (309).
65. Klunk WE; Xu CJ; McClure RJ; Panchalingam K; Stanley JA; Pettegrew JW Aggregation of beta-amyloid peptide is promoted by membrane phospholipid metabolites elevated in Alzheimer's disease brain. J Neurochem 1997, 69 (1), 266–72. [PubMed: 9202319]
66. Chew H; Solomon VA; Fonteh AN Involvement of Lipids in Alzheimer's Disease Pathology and Potential Therapies. Frontiers in Physiology 2020, 11 (598).
67. Kao Y-C; Ho P-C; Tu Y-K; Jou IM; Tsai K-J Lipids and Alzheimer's Disease. Int J Mol Sci 2020, 21 (4), 1505.
68. Hughes C; Gaunt L; Brown M; Clarke NW; Gardner P Assessment of paraffin removal from prostate FFPE sections using transmission mode FTIR-FPA imaging. Analytical Methods 2014, 6 (4), 1028–1035.
69. Kumar S; Lemere CA; Walter J Phosphorylated Aβ peptides in human Down syndrome brain and different Alzheimer's-like mouse models. Acta Neuropathologica Communications 2020, 8 (1), 118. [PubMed: 32727580]
70. Kumar S; Walter J Phosphorylation of amyloid beta (Aβ) peptides – A trigger for formation of toxic aggregates in Alzheimer's disease. Aging 2011, 3 (8), 803–812. [PubMed: 21869458]
71. Dzamba D; Harantova L; Butenko O; Anderova M Glial Cells - The Key Elements of Alzheimeŕs Disease. Curr Alzheimer Res 2016, 13 (8), 894–911. [PubMed: 26825092]
72. Hong JH; Kang JW; Kim DK; Baik SH; Kim KH; Shanta SR; Jung JH; Mook-Jung I; Kim KP Global changes of phospholipids identified by MALDI imaging mass spectrometry in a mouse model of Alzheimer's disease. Journal of Lipid Research 2016, 57 (1), 36–45. [PubMed: 26538545]
73. Zhang X; Liu W; Zan J; Wu C; Tan W Untargeted lipidomics reveals progression of early Alzheimer's disease in APP/PS1 transgenic mice. Scientific Reports 2020, 10 (1), 14509. [PubMed: 32884056]
74. Tokuoka SM; Kita Y; Shimizu T; Oda Y Isobaric mass tagging and triple quadrupole mass spectrometry to determine lipid biomarker candidates for Alzheimer's disease. PLOS ONE 2019, 14 (12), e0226073. [PubMed: 31821352]
75. Ji M; Arbel M; Zhang L; Freudiger CW; Hou SS; Lin D; Yang X; Bacskai BJ; Xie XS Label-free imaging of amyloid plaques in Alzheimer's disease with stimulated Raman scattering microscopy. Science Advances 2018, 4 (11), eaat7715. [PubMed: 30456301]

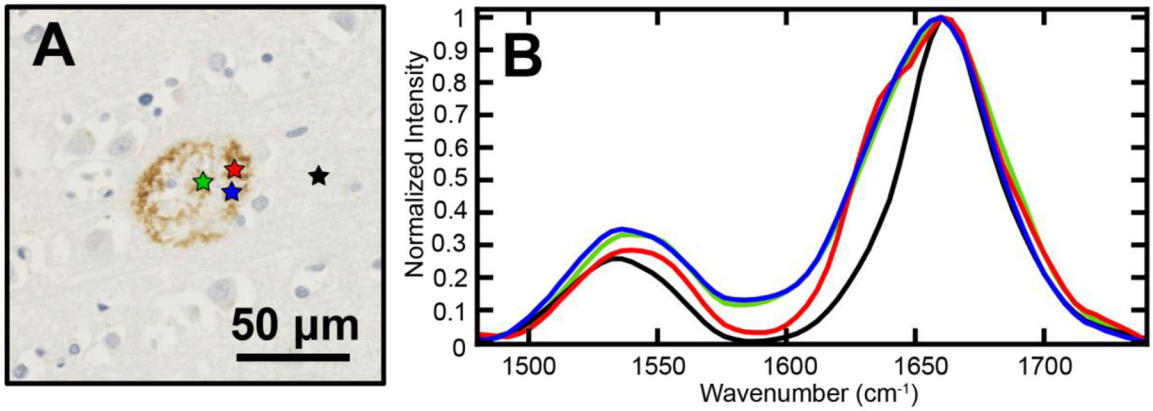

Figure 1.

Representative IHC stained plaque from diseased precentral gyrus tissue (A) and spectra (B) from outside the plaque area (black) and inside the plaque area (red, green, blue). The spatial locations of the spectra are indicated with stars (color matched to spectra).

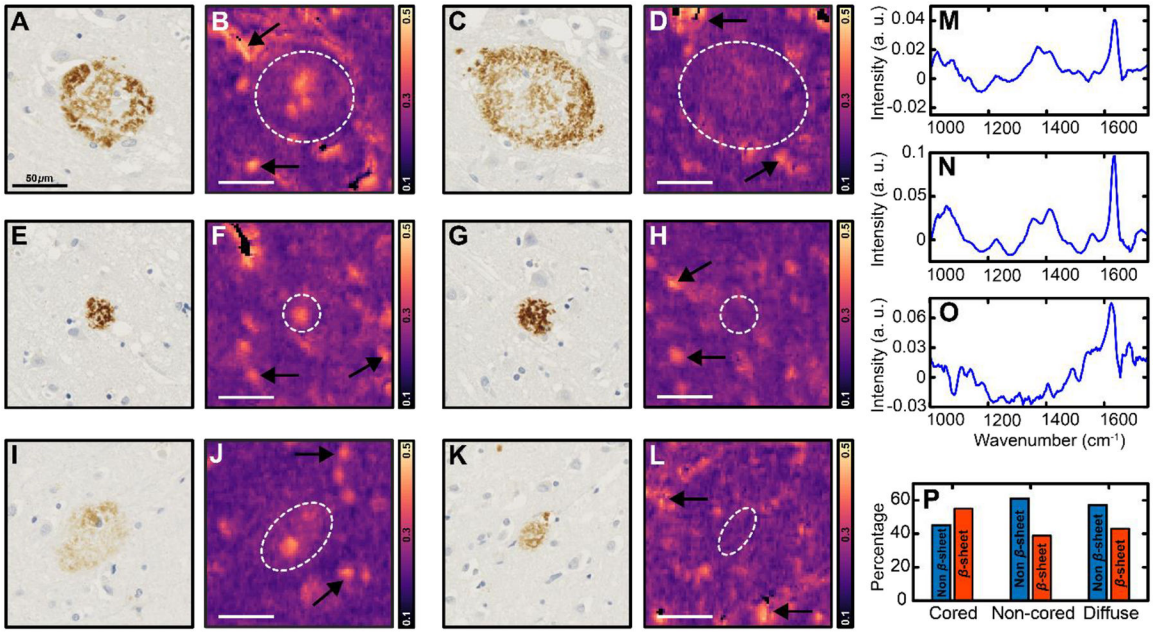

Figure 2.

Diseased precentral gyrus IHC images (A, C, E, G, I, K) and beta sheet ratio IR images (yellow indicates increased beta sheet character) (B, D, F, H, J, L) of cored neuritic plaques (A-D), non-cored plaques (E-H), and diffuse plaques (I-L) with beta sheet (A, B, E, F, I, J) and without significant beta sheet (C, D, G, H, K, L) content and mean normalized plaque IR difference spectra for cored neuritic plaques (M), non-cored plaques (N), and diffuse plaques (O). The scalebars are equal to 50 microns. The dashed circles indicate the plaque boundaries as identified from the IHC stained images. The arrows indicate beta sheet deposits outside of plaques, discussed later in the manuscript. The percentage of each of plaque subtype (cored, non-cored and diffuse) classified as beta sheet containing (red bars) or beta sheet depleted (blue bars) is shown in Figure 2P.

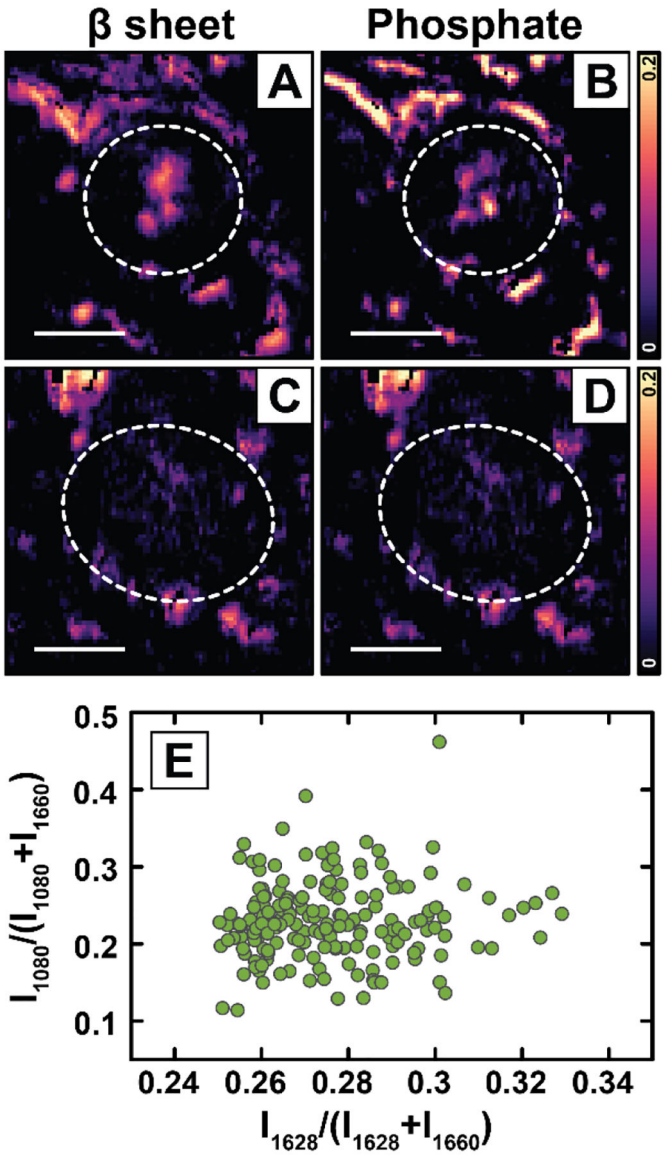

Figure 3.

Beta sheet (A, C) and phosphate (B, D) ratio images of precentral gyrus IHC stained cored plaques from Figure 2. The scalebars are equal to 50 microns. (E) Scatter plot of phosphate vs beta sheet intensities from plaque spectra from all three tissue specimens (precentral gyrus, postcentral gyrus, and occipital lobe).

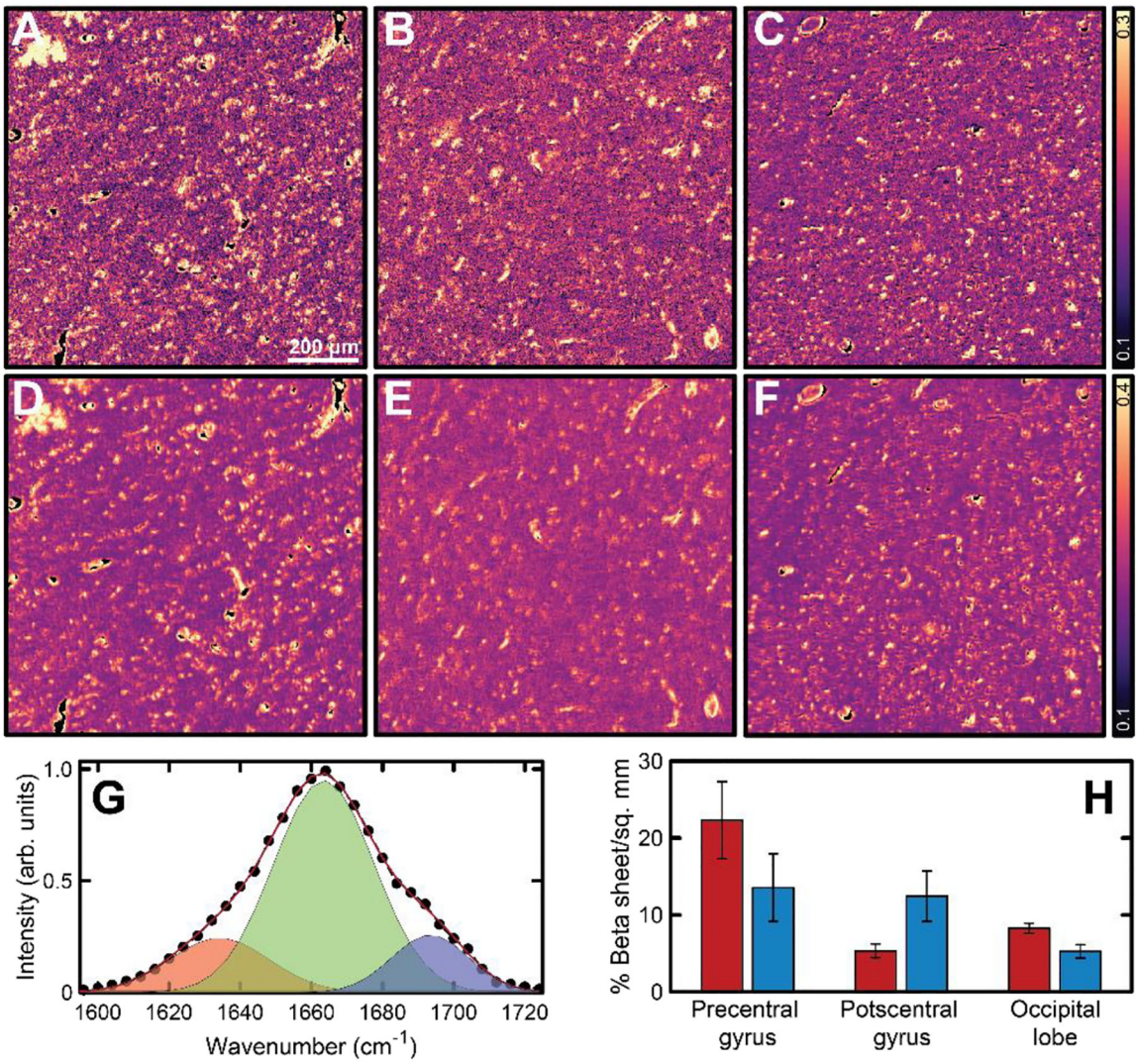

Figure 4.

3 peak fitted peak intensity beta sheet ratio (A, B, C) and spectral intensity beta sheet ratio (D, E, F) for diseased precentral gyrus (A, D), postcentral gyrus (B, E), and occipital lobe (C, F). Scale bar: 200 microns. A representative spectral fit is shown in (G). The red line corresponds to the fit; the black circles correspond to measured spectrum. The average percentage of beta sheet rich pixels per square mm in the diseased (red) and normal (blue) tissues is shown in (H).

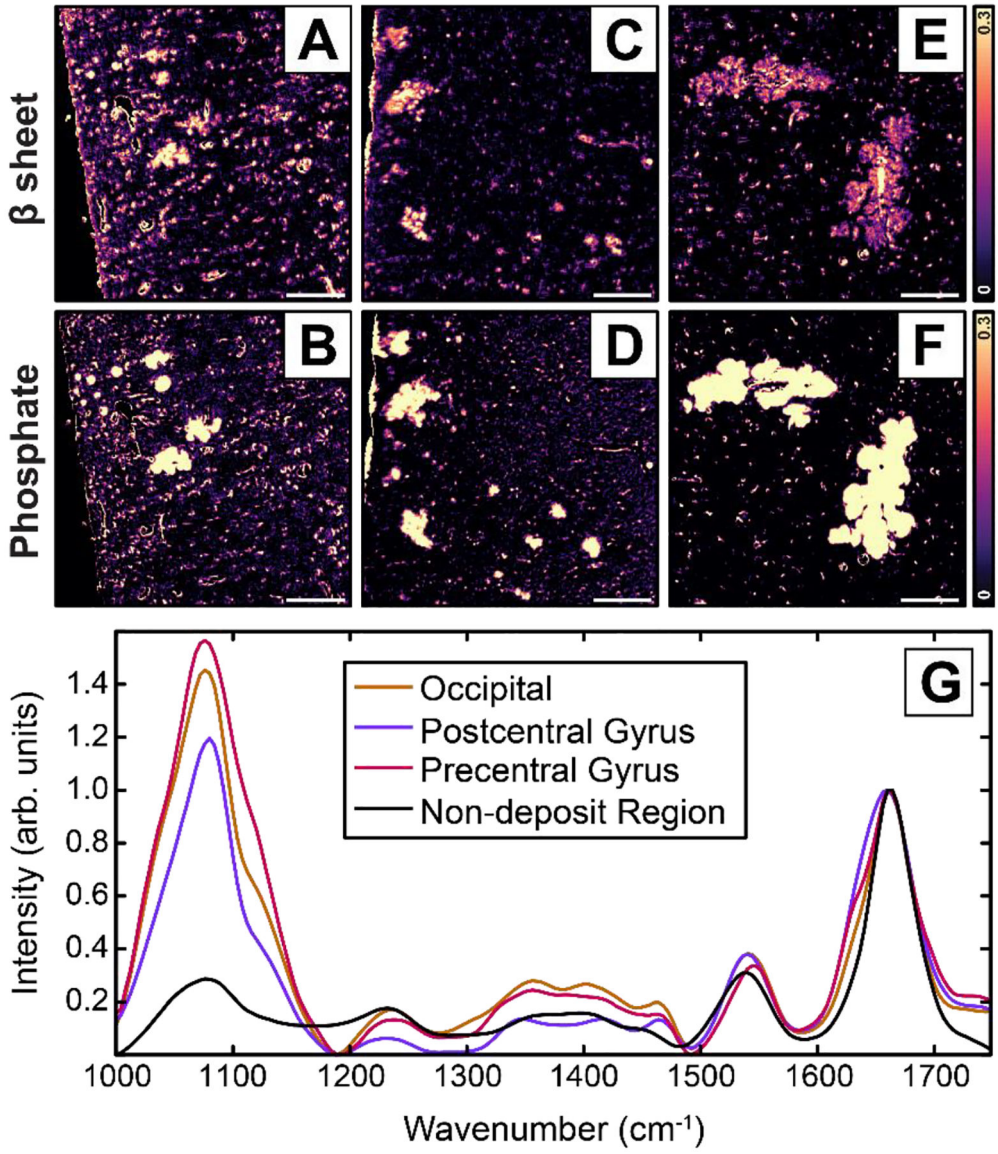

Figure 5.

Beta sheet (A, C, E) and phosphate (B, D, F) ratio images of non-plaque areas showing high phosphate concentration for diseased precentral gyrus (A-B), postcentral gyrus (C-D), and occipital lobe (E-F). Scale bar: 200 microns. Representative spectra from these deposits are shown in (G). For each image, the corresponding mean value was subtracted for clarity.

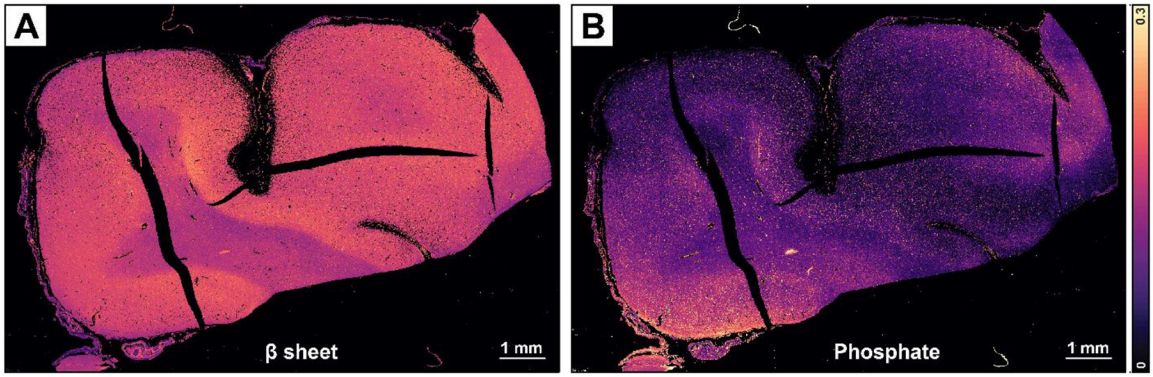

Figure 6.

Beta sheet (A) and phosphate (B) ratio images of a normal brain tissue section (frontal lobe). For each image, the corresponding mean value has been subtracted for clarity. Absorptions at only three wavenumbers need to be recorded (~40 minutes per map) to generate the above images. This makes the DFIR approach significantly faster than conventional FTIR microscopy and enables investigation of large tissue sections.